RMetS

Royal Meteorological Society

Stably stratified airflow over a waved water surface. Part 1: Stationary turbulence regime

O. A. Druzhinin,[a,b*] Y. I. Troitskaya[a,b,c] and S. S. Zilitinkevich[b,d,e,f,g]

[a]*Institute of Applied Physics, Russian Academy of Sciences, Ul'anov str. 46, Nizhny Novgorod, 603950 Russia*
[b]*Radiophysics Department, University of Nizhny Novgorod, Russia*
[c]*Institute of Physics of the Atmosphere, Russian Academy of Sciences, Moscow, Russia*
[d]*Physics Department, Moscow State University, Moscow, Russia*
[e]*Institute of Geography, Russian Academy of Sciences, Moscow, Russia*
[f]*Finnish Meteorological Institute, Helsinki, Finland*
[g]*Division of Atmospheric Sciences, University of Helsinki, Finland*

Correspondence to: O. A. Druzhinin. Institute of Applied Physics, Russian Academy of Sciences, Ul'anova str. 46, Nizhny Novgorod, 603950 Russia. E-mail: druzhinin@hydro.appl.sci-nnov.ru

Stably stratified turbulent boundary-layer flows over both a waved water surface and a flat smooth surface are investigated through direct numerical simulation (DNS) for the bulk Reynolds numbers, *Re*, from 15 000 to 80 000. DNS expose the following basic properties of the flow. A statistically stationary turbulent regime is sustained if the turbulent Reynolds number, Re_L, based on the Obukhov length-scale and friction velocity, is larger than 10^2. At $Re_L < 10^2$, turbulence over a flat surface degenerates completely, but over a waved surface it survives in the form of residual fluctuations, which are weaker for smaller wave slopes. In the stationary turbulent regime, at $Re_L > 10^2$, vertical profiles of the mean-flow velocity and temperature have a log-linear shape, as predicted by the Monin-Obukhov similarity theory, with the same empirical dimensionless constants as in laboratory and field experiments. The velocity and temperature roughness lengths, vertical turbulent fluxes of momentum and heat, and root mean square turbulent velocity and temperature fluctuations increase with increasing slope of the surface waves. At the same time, vertical profiles of the mean velocity and temperature keep the self-similar shape predicted by the Monin−Obukhov theory, irrespective of the wave slope.

Key Words: direct numerical simulation; stable stratification; turbulent airflow; waved water surface

Received 25 March 2015; Revised 14 September 2015; Accepted 21 September 2015; Published online in Wiley Online Library

1. Introduction

Detailed knowledge of the physical mechanisms of interaction between airflow and surface waves is of primary importance for realistic representation of vertical turbulent fluxes of momentum, energy and matter, linking the atmosphere and hydrosphere in climate and weather prediction model systems. In state-of-the-art models, these fluxes are calculated via bulk formulae to a large extent based on empirical coefficients. The latter are obtained from field and laboratory experiments and exhibit essential variability, whose nature in relation to wind-wave interaction processes is not yet fully understood (Fairall *et al.*, 2003). Of special interest is the influence of stratification in the atmospheric surface layer on wind-wave interactions and the air-sea fluxes.

Measurements above a waved water surface require special efforts. Especially complicated are measurements in wave troughs and in a thin layer above the water surface covering the viscous sublayer and the adjacent buffer layer. The typical height of the region to be examined is of order of millimetres, which is usually much smaller than the surface wave amplitude. Here, detailed properties of airflow cannot be detected using contact measurement techniques, such as wave-following probes (Hsu *et al.*, 1981; Hsu and Hsu, 1983; Donelan *et al.*, 2005). However, methods based on the particle image velocimetry (PIV) technique (Adrian, 1991) allow for measuring wind velocity at heights over the surface of order 1 mm. This is sufficient for investigating both viscous and buffer layers at not too strong winds, with friction velocities less than $10\,\mathrm{cm\,s^{-1}}$ (Reul, 1999; Veron *et al.*, 2007; Troitskaya *et al.*, 2011). Precise measurements of the air temperature in the viscous sublayer and buffer layer above waves are strongly needed but still remain difficult.

Numerical experiments make a complementary tool to laboratory and field measurements. Earlier numerical modelling of interaction between turbulent airflow and surface waves was based on the Reynolds (ensemble) Averaged, Navier-Stokes (RANS) equations for stationary, two-dimensional flow (Gent and Taylor, 1976; Al-Zanaidi and Hui, 1984; Chalikov, 1986). These RANS equations employed the semi-empirical concept

of turbulent viscosity to express unknown Reynolds (turbulent) stresses through known mean-field gradients. This approach is computationally cheap and provides a useful picture of the mean velocity, pressure and turbulent fluxes in the airflow. However, it is not immediately applicable to modelling airflow in the viscous sublayer and buffer region, which requires inclusion of the molecular transports (L'vov *et al.*, 2006).

More advanced (but more computationally expensive) is Large-Eddy Simulation (LES) based on numerical integration of three-dimensional, non-stationary, filtered Navier-Stokes equations and capable of resolving 3D large-scale turbulent structure of the flow (cf. Sullivan *et al.*, 2008, 2014). However, LESs do not resolve properties of the flow close to the water surface (or solid wall). Typically the first LES grid node in the vertical direction is located within the logarithmic region of the boundary layer. As a remedy, one can perform *wall-resolved* LES (cf. Pope, 2000) and resolve the viscous sublayer; however, numerical costs strongly increase.

Direct Numerical Simulation (DNS) is free of this drawback and resolves the entire turbulence spectrum from large eddies down to the dissipation length-scale. Sullivan *et al.* (2000) were the first who employed DNS to investigate *non-stratified* turbulent wind flow over surface waves for bulk Reynolds number $Re = (U_0 \lambda / \nu) = 8800$ (where U_0 is the bulk wind flow velocity, λ the surface wave length, and ν the air molecular viscosity) and wave slope $ka = 0.1$ (where k is the wavenumber and a the wave amplitude). In their follow-up study, Sullivan and McWilliams (2002) performed DNS of the airflow above the surface waves in the presence of both stable and unstable stratification, with the same wave slope ($ka = 0.1$) and somewhat lower Reynolds number ($Re = 8000$). Later Yang and Shen (2010) performed DNS study of turbulent, non-stratified flow over waves with maximum slope $ka = 0.25$ and $Re \approx 10\,000$. Although DNS provides a full description of the turbulent flow at all physically significant scales, so far it has not been able to achieve Reynolds numbers of order 10^5 typical of the wind-wave interaction in laboratory experiments. Druzhinin *et al.* (2012) have performed DNS of non-stratified turbulent flow over waved water surface for $Re = 15\,000$ – almost twice that of the $Re = 8800$ approached by Sullivan *et al.* (2000) and 50% larger than $Re = 9943$ approached by Yang and Shen (2010), with maximum wave slope $ka = 0.2$ – close to 0.25 approached by Yang and Shen (2010).

In the present study, we consider the *stably stratified* airflows over a waved water surface with wave slopes up to $ka = 0.2$ and bulk Reynolds numbers from $Re = 15\,000$ up to $Re = 80\,000$ and for different bulk Richardson numbers, Ri (based on the mean wind velocity and temperature difference, and the wave length λ). To the best of our knowledge, this is the first DNS study of the stably stratified boundary-layer flow with such high Reynolds numbers (up to $Re \sim 10^5$) over *waved water* surface. The results obtained in DNS studies of the stably stratified boundary layers over a *flat* surface (e.g. Coleman *et al.*, 1992; Nieuwstadt, 2005; García-Villalba and del Álamo, 2011; Flores and Riley, 2011; Ansorge and Mellado, 2014; Deusebio *et al.*, 2014) show that increasing stratification leads to transition from a stationary turbulent regime, in weak stratification, to a laminar flow regime in sufficiently strong stratification. We focus on the stationary turbulent regime observed for a sufficiently small Ri (cf. Sullivan and McWilliams, 2002). Degeneration of turbulence at larger Ri and the problem of transition between turbulent and laminar regimes is considered in our follow-up study (Druzhinin *et al.*, 2015, Part 2).

2. Basic equations and numerical method

We perform direct numerical simulation of turbulent stably stratified Couette flow above waved water surface. The schematic of the numerical experiment is similar to the one used by Sullivan and McWilliams (2002) (Figure 1). A Cartesian framework is considered where x-axis is oriented along the mean wind, z-axis is directed vertically upwards and y-axis is orthogonal

to the mean flow and parallel to the wave front. We prescribe two-dimensional, x-periodic water wave with amplitude a, wavelength λ and phase velocity c. The maximum wave slope considered in our DNS is $ka = 2\pi a/\lambda = 0.2$. The rectangular computational domain has the sizes $L_x = 6\lambda$, $L_y = 4\lambda$ and $L_z = \lambda$ in the x-, y-, and z-directions, respectively, and the airflow is assumed to be periodic in the x- and y-directions. DNS is performed in a reference frame moving with the wave phase velocity, c, so that the horizontal coordinate in the moving framework is $x = x' - ct$, where x' is the coordinate in the laboratory reference frame. Then the lower boundary, representing the wave surface, is stationary in the moving reference frame. As in all previous DNS studies mentioned above, in the present DNS study we do not consider capillary ripples riding on the wave generally found in a realistic sea situation. The presence of ripples increases the effective wavy-surface slope and may cause local flow separation which significantly complicates numerical solution. The no-slip boundary condition is prescribed at the lower boundary, so that the wind velocity at the boundary coincides with the velocity in the water wave. The no-slip boundary condition is also prescribed at the upper horizontal plane moving in x-direction with bulk velocity U_0. This condition provides the external source of momentum due to the viscous shear stress, which compensates the viscous dissipation in the boundary layer and makes the flow statistically stationary. The stable density stratification is specified by prescribing the potential temperature at the wavy surface as $\Theta = \Theta_0$ and the top boundary plane as $\Theta = \Theta_0 + \Delta\Theta$, where $\Delta\Theta > 0$.

Numerical algorithm is based on the integration of full, 3D Navier-Stokes equations for incompressible fluid under the Boussinesq approximation (Monin and Yaglom, 1971):

$$\frac{\partial U_i}{\partial t} + \frac{\partial (U_i U_j)}{\partial x_j} = -\frac{\partial P}{\partial x_j} + \nu \frac{\partial^2 U_i}{\partial x_j \partial x_j} + \delta_{iz} \frac{g}{\Theta_0}(\Theta - \Theta_{ref}), \quad (1)$$

$$\frac{\partial U_j}{\partial x_j} = 0, \quad (2)$$

$$\frac{\partial \Theta}{\partial t} + \frac{\partial (U_j \Theta)}{\partial x_j} = \frac{\nu}{Pr} \frac{\partial^2 \Theta}{\partial x_j \partial x_j}, \quad (3)$$

where $x_i = x, y, z$, $U_i (i = x, y, z)$ are the velocity components, P is pressure and Θ_{ref} is the reference temperature, ν is the kinematic air viscosity and g the gravity acceleration. The Prandtl number, $Pr = \nu/\mu$ (where μ is thermal diffusivity).

The integration is performed in curvilinear coordinates (ξ, y, η) which are related to the Cartesian coordinates (x, y, z) by the mapping:

$$x = \xi - a \exp(-k\eta) \sin k\xi, \quad (4)$$

$$z = \eta + a \exp(-k\eta) \cos k\xi. \quad (5)$$

This mapping transforms the lower waved boundary $z_b(x) = a \cos k\xi(x)$ into a plane boundary at $\eta = 0$ (Druzhinin *et al.*, 2012). It is easy to show that for a small, finite wave amplitude a, the shape of the boundary, $z_b(x)$, up to the terms of order $O(k^2 a^3)$, coincides with asymptotic solution for the Stokes wave (Gent and Taylor, 1976):

$$z_b(x) = a \cos kx + \frac{1}{2} a^2 k (\cos 2kx - 1). \quad (6)$$

The governing equations (1)–(3) are rewritten in dimensionless variables normalized by the wavelength λ, bulk velocity U_0 and temperature difference $\Delta\Theta$, and pressure normalized by ρU_0^2 (where ρ is the air density). The integration is performed using dimensionless curvilinear coordinates, $\xi_1 = \xi/\lambda, \xi_2 = y/\lambda, \xi_3 = \eta/\lambda$, and Cartesian velocity components $U_1 = U_x/U_0$, $U_2 = U_y/U_0$, and $U_3 = U_z/U_0$. We also introduce a linear reference temperature profile, $\Theta_{ref}(\xi_2) = \Delta\Theta \eta/\lambda$, and perform the integration with respect to the dimensionless deviation of the temperature, $\widetilde{T} = (\Theta - \Theta_{ref})/\Delta\Theta$. The dimensionless governing equations solved in DNS are given in the Appendix.
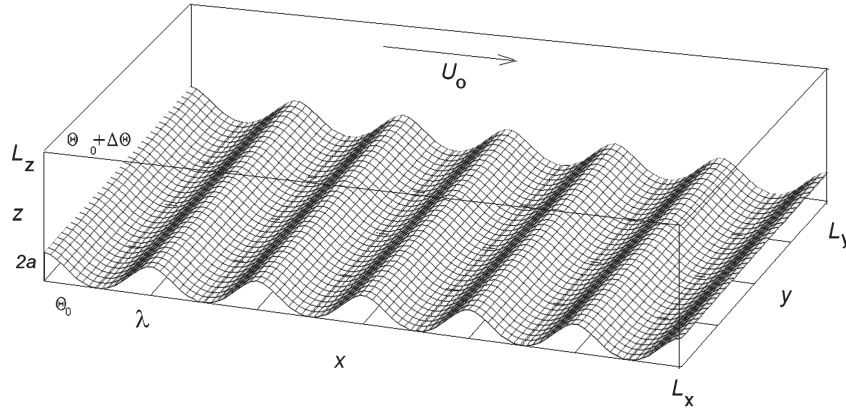
Figure 1. Schematic of the numerical experiment.

Table 1. Parameters of DNS runs.

Re	Ri	$\Delta\xi_1^+$	$\Delta\xi_3^{w+}$	Re_τ	Re_L	ka	c/U_0	State
15 000	0.04	5.21	0.26	315	304	0	0	Turb.
15 000	0.06	4.8	0.24	280	230	0	0	Turb.
15 000	0.04	6.1	0.31	360	310	0.2	0.2	Turb.
15 000	0.04	5.6	0.28	330	290	0.1	0.05	Turb.
15 000	0.04	6.3	0.31	375	350	0.2	0.05	Turb.
30 000	0.075	6.9	0.35	410	160	0	0	Turb.
40 000	0.09	7.2	0.36	430	120	0	0	Turb.
40 000	0.1	8.3	0.42	520	160	0.2	0.05	Turb.
80 000	0.11	10.4	0.56	650	105	0	0	Turb.
15 000	0.08	–	–	–	–	0.2	0.05	Pre-turb.
40 000	0.2	–	–	–	–	0.2	0.05	Pre-turb.
80 000	0.2	–	–	–	–	0.15	0.05	Pre-turb.

The governing parameters in DNS are the bulk Reynolds and Richardson numbers defined as:

$$Re = \frac{U_0\lambda}{\nu}, \qquad (7)$$

$$Ri = g\frac{\Delta\Theta}{\Theta_0}\frac{\lambda}{U_0^2}. \qquad (8)$$

The Prandtl number, $Pr = \nu/\mu$ (where μ is thermal diffusivity), is prescribed as $Pr = 0.7$.

The governing equations are discretized in a rectangular domain with sizes $0 < \xi_1 < 6$, $0 < \xi_2 < 4$, and $0 < \xi_3 < 1$ by employing a finite-difference method of second-order accuracy on a uniform staggered grid consisting of $360 \times 240 \times 180$ nodes. An additional mapping is employed to compress the grid in the vertical direction near the boundaries in order to resolve the viscous boundary layer (cf. Appendix). Parameters of DNS runs are listed in the Table 1. Note that the relatively high Reynolds number in the present study required sufficiently high resolution of the fine scales where dissipation of turbulent kinetic energy occurs in DNS. In the considered case of boundary-layer flow, the viscous scale is ν/u_*, where u_* is the friction velocity and ν the kinematic viscosity. This scale generally varies in DNS for different bulk Reynolds numbers and Richardson numbers. Our DNS employ the grid with mesh sizes $\Delta\xi_1 = 1/60$ in the streamwise and spanwise directions, ξ_1 and ξ_2, whereas in the vertical direction ξ_3 the mesh size increases from $\Delta\xi_3^w \approx 0.0008$ near the walls to $\Delta\xi_3^c \approx 0.009$ in the centre of computational domain. When normalized by the wall scale, the mesh sizes for different Re and Ri vary as $\Delta\xi_1^+ \approx 2 \div 10$ in the horizontal plane and from $\Delta\xi_3^{w+} \approx 0.2 \div 0.6$ near the boundaries to about $\Delta\xi_3^{c+} \approx 2 \div 5$ in the centre of the domain. These grid spacings are generally regarded as sufficient to resolve fine-scale turbulent motions in DNS of turbulent boundary-layer flows (as discussed by Moin and Manesh, 1998). In the DNS runs listed in the three bottom rows of Table 1, the flow relaminarizes and turbulent fluxes of momentum and heat drastically reduce in the bulk of

the computational domain. In this regime, finite velocity and temperature fluctuations survive only in the vicinity of the waved surface and vanish sufficiently far from the surface. We propose for these wave-induced motions observed near the waved surface the name 'pre-turbulent motions'. This regime is only briefly discussed in the present article and investigated in detail in our follow-up article (Druzhinin *et al.*, 2015, Part 2).

The numerical method used in the present study takes into account the effect of stratification and solves both the Navier-Stokes equations for the fluid velocity and the temperature deviation equation (Appendix). Otherwise, the method is quite similar to that employed in the non-stratified case by Druzhinin *et al.* (2012). In this case, we validated our numerical code by comparison with both available laboratory data and DNS results by Sullivan *et al.* (2000).

At the lower-plane boundary ($\xi_3 = 0$), the no-slip (Dirichlet) condition for the velocity is prescribed. Thus, the airflow velocity here coincides with the velocity of the water in the surface wave:

$$U_1(\xi_1, \xi_2, 0) = c(ka\cos kx_1(\xi_1, \xi_3) - 1), \qquad (9)$$

$$U_2(\xi_1, \xi_2, 0) = 0, \qquad (10)$$

$$U_3(\xi_1, \xi_2, 0) = cka\sin kx_1(\xi_1, \xi_3). \qquad (11)$$

At the upper boundary ($\xi_3 = 1$), the no-slip condition for the wind velocity is prescribed with respect to the plane moving with non-dimensional velocity ($1 - c$):

$$U_1(\xi_1, \xi_2, 1) = 1 - c, \qquad (12)$$

$$U_2(\xi_1, \xi_2, 1) = 0, \qquad (13)$$

$$U_3(\xi_1, \xi_2, 1) = 0. \qquad (14)$$

The temperature deviation is set equal to 0 at both lower and upper boundaries:

$$\widetilde{T}(\xi_1, \xi_2, 0) = \widetilde{T}(\xi_1, \xi_2, 1) = 0. \qquad (15)$$

Periodical boundary conditions are prescribed at the side boundaries of the computational domain, namely at $\xi_1 = 0, 6$ and $\xi_2 = 0, 4$.

The velocity field is initialized as a weakly perturbed laminar Couette flow, $U_i = \xi_3\delta_{i1} + u_{if}$ ($i = 1, 2, 3$) where u_{if} is a divergence-free isotropic, homogeneous random field with a broad power spectrum and the modulus amplitude 0.05. The initial temperature deviation field is put to 0. During the transient, at times $t < 100$, the effect of stratification is artificially delayed and negligible (cf. Appendix). By this means, a fully developed, non-stratified turbulent regime is allowed to set in. At later times, the buoyancy force becomes significant and modifies the airflow. The integration is advanced in time until a statistically stationary flow regime is established. Then sampling of the velocity and temperature fields is performed at discrete time moments $t_k, k = 1, \ldots, 1000$, with interval $t_{k+1} - t_k = 0.2$. The averaging over the wave length is performed as a window averaging.

We denote by the angular brackets the *phase* averaging equivalent to averaging over turbulent fluctuations, i.e. for a given field $f(\xi_1, \xi_2, \xi_3, t)$, the phase-averaged field, $\langle f \rangle$, and dispersion field, $\langle f^2 \rangle$, are determined as:

$$\langle f \rangle(\xi_1, \xi_3) = \frac{1}{6N_t N_y} \sum_{j=1}^{N_y} \sum_{k=1}^{N_t} \sum_{n=0}^{5} f(\xi_1 + n\lambda, \xi_{2j}, \xi_3, t_k), \quad (16)$$

$$\langle f^2 \rangle(\xi_1, \xi_3) = \frac{1}{6N_t N_y} \sum_{j=1}^{N_y} \sum_{k=1}^{N_t} \sum_{n=0}^{5} f^2(\xi_1 + n\lambda, \xi_{2j}, \xi_3, t_k), \quad (17)$$

where $N_y = 240$, $N_t = 500$ and $0 < \xi_1 < 1$. The fluctuation of the field f is further obtained in the form:

$$f' = (\langle f^2 \rangle - \langle f \rangle^2)^{1/2}. \quad (18)$$

We also introduce rectangular brackets for the *mean* vertical profile of the field f, $[f](\xi_3)$, obtained by additional averaging of the phase-average $\langle f \rangle(\xi_1, \xi_3)$ along the streamwise coordinate:

$$[f](\xi_3) = \frac{1}{N_x} \sum_{k=1}^{N_x/6} \langle f \rangle(\xi_{1k}, \xi_3), \quad (19)$$

where $N_x = 360$. Then, vertical profiles of mean turbulent fluxes of momentum and heat, $\tau(\xi_3)$ and $F(\xi_3)$, are determined as

$$\tau = [\langle U_1 \rangle \langle U_3 \rangle - \langle U_1 U_3 \rangle], \quad (20)$$

$$F = [\langle \widetilde{T} \rangle \langle U_3 \rangle - \langle \widetilde{T} U_3 \rangle], \quad (21)$$

We define the conventional turbulent velocity and temperature scales, namely, u_* (friction velocity measured in m s^{-1}) and Θ_* (measured in K) expressed through the dimensionless turbulent fluxes, τ and F (Eqs (20) and (21)), as

$$u_* = U_0\sqrt{\tau}, \Theta_* = \Delta\Theta F/\sqrt{\tau}, \quad (22)$$

where τ and F are taken at *sufficiently large* distance from the waved surface, where they reach asymptotically constant values. The Obukhov turbulent length-scale L (measured in m) is:

$$L = \frac{u_*^2}{(g/\Theta_0)\Theta_*}. \quad (23)$$

Note that traditional definition of the Obukhov length includes the von Kármán constant, κ, known only approximately, in the denominator on the r.h.s. of Eq. (23). We do not follow this tradition because it causes additional uncertainties in empirical dependencies on z/L.
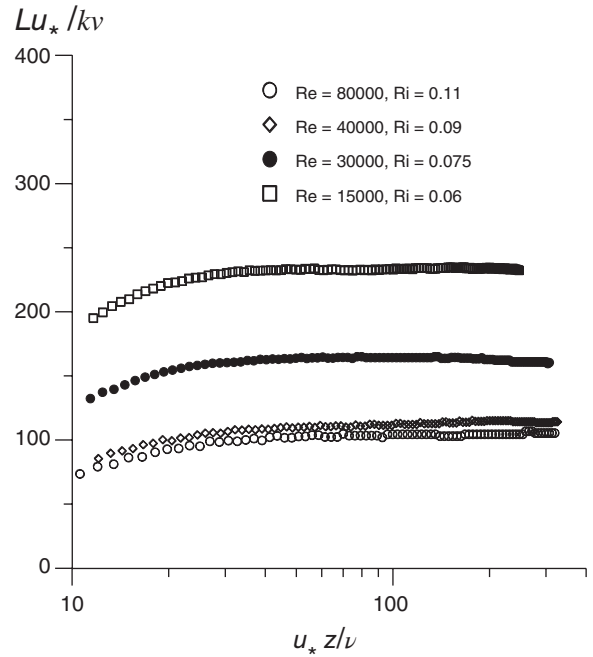

Figure 2. Vertical profiles of the turbulent Reynolds number Re_L (Eq. (24)) in DNS of stably stratified flows over a flat surface for different Reynolds and Richardson bulk numbers.

3. The effect of stratification on turbulent flow regimes over flat and waved surfaces

The particular case of stably stratified turbulent flow over a smooth flat surface can be investigated with the aid of the DNS procedure described in section 2 by setting zero values of the phase velocity, $c = 0$, and wave slope, $ka = 0$. We performed such DNS for the bulk Reynolds number, Re, defined by Eq. (7), from 15 000 to 80 000 and bulk Richardson number, Ri, Eq. (8), from 0 to 0.5 (cf. Table 1). At sufficiently small Ri, DNS reproduces a statistically stationary turbulent regime with vertical profiles of mean velocity and temperature obeying the Monin-Obukhov similarity theory. At large Ri, turbulence degenerates. We investigated the transition from the turbulent to the laminar regime as dependent on both Reynolds and Richardson numbers, and compared our results with those of the previous study by Flores and Riley (2011). These authors compiled available laboratory and numerical data and performed DNS of their own to analyse the transition from turbulent to laminar regime in terms of the *turbulent Reynolds number*, Re_L, based on the Obukhov length-scale and friction velocity:

$$Re_L = \frac{Lu_*}{\kappa\nu}. \quad (24)$$

Note that, in Eq. (24), we included the von Kármán constant, $\kappa = 0.4$, in the denominator, as compared to the original definition of Re_L by Flores and Riley (2011), to account for the absence of κ in the definition of the Obukhov length L in Eq. (23).

The basic result obtained by Flores and Riley (2011) is that the stationary turbulent regime is maintained at $Re_L > 100$; otherwise turbulence degenerates and the flow becomes laminar. Our DNS confirms this conclusion. Figure 2 presents vertical profiles of the turbulent Reynolds number, Re_L, for different *bulk Reynolds numbers*: $Re = 15\,000$, $30\,000$, $40\,000$, and $80\,000$. For each Re, we determined appropriate critical Richardson number, Ri_c, such that for $Ri > Ri_c$ turbulence degenerated. Then we considered vertical profiles of Re_L for Ri close to Ri_c. As seen in Figure 2, at sufficiently large *bulk Reynolds numbers* ($Re = 40\,000$ and $80\,000$), the *turbulent Reynolds number*, Re_L, asymptotically tends to the threshold value $Re_L \approx 100$ found by Flores and Riley (2011).

We note that Flores and Riley (2011) used the constant heat flux condition (which implied cooling), whereas we use the prescribed
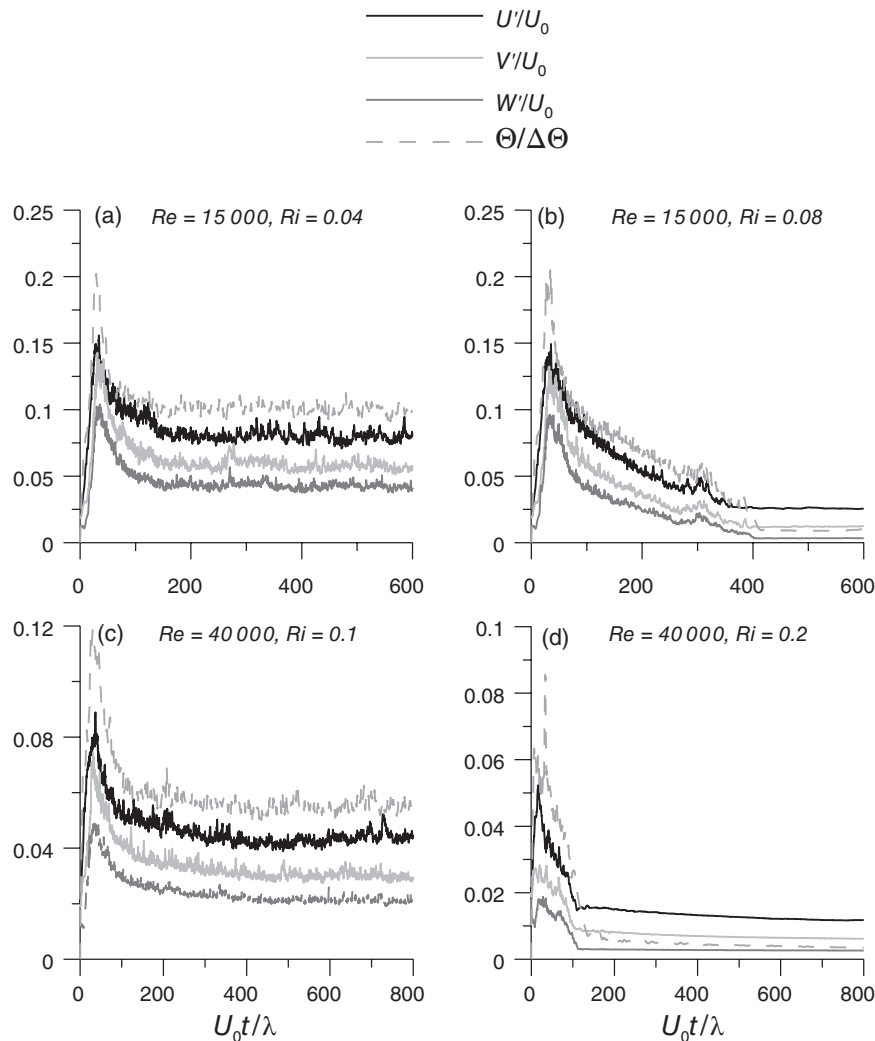
Legend:
— U'/U_0
— V'/U_0
— W'/U_0
– – – $\Theta/\Delta\Theta$

(a) $Re = 15\,000$, $Ri = 0.04$
(b) $Re = 15\,000$, $Ri = 0.08$
(c) $Re = 40\,000$, $Ri = 0.1$
(d) $Re = 40\,000$, $Ri = 0.2$

$U_0 t/\lambda$

Figure 3. Temporal development of root mean square fluctuations of velocity (U', V', W') and temperature (Θ') in stably stratified boundary-layer flows over waved surfaces, obtained in DNS for different bulk Reynolds, Re, and Richardson, Ri, numbers at the wave slope $ka = 0.2$ and dimensionless phase velocity $c/U_0 = 0.05$. (a,c) Represent the fully developed turbulence regime under subcritical stable stratification, whereas (b,d) show the wave-induced residual-turbulence regime under strongly stable (supercritical) stratification.

temperature at the surface. However, the boundary condition for temperature does not directly influence the above criterion: $Re_L < 10^2$. The physical meaning of this criterion is quite clear: the Reynolds number should be large enough (and hence, the viscous damping small enough) to allow for the existence of turbulent motions. The key point is that Flores and Riley (2011) have found for the flow in question the *relevant velocity- and length-scales*: u_* and L. They have shown that the criterion obtained in their DNS explains the transition from a stationary turbulent to a laminar regime observed both in field experiments and previous numerical studies where the isothermal (fixed temperature) condition at the surface was considered as well.

We performed DNS of stably stratified flows over waved surface for the wave slope $0 < ka < 0.2$, bulk Reynolds number $15\,000 < Re < 40\,000$, bulk Richardson number $0 < Ri < 0.1$, and different phase velocities c. Our DNS reveal quite similar control of the flow regime by Ri. Figure 3 shows temporal variation of the amplitudes of turbulent fluctuations of wind velocity (U', V', W') and temperature (Θ'), defined as maxima of the corresponding fluctuation fields obtained from Eq. (18),

$$U', V', W' \equiv U_0 \max\{U_i'\}, i = 1, 2, 3; \ \Theta' \equiv \Delta\Theta \max\{\widetilde{T'}\}, \quad (25)$$

in DNS with the wave slope $ka = 0.2$ and dimensionless wave phase velocity $c/U_0 = 0.05$ for the two bulk Reynolds numbers $Re = 15\,000$ (a,b) and $Re = 40\,000$ (c,d), and four Richardson numbers: $Ri = $ (a) 0.04, (b) 0.08, (c) 0.1, and (d) 0.2. At sufficiently small Richardson numbers ($Ri = 0.04$ for $Re = 15\,000$

(Figure 3(a)), and $Ri = 0.1$ for $Re = 40\,000$ (Figure 3(c)), the amplitudes of fluctuations, after initial transients, saturate, so that a stationary turbulent regime sets in. At larger Richardson number ($Ri = 0.08$ for $Re = 15\,000$ in Figure 3(b), and $Ri = 0.2$ for $Re = 40\,000$ in Figure 3(d)), the amplitudes of fluctuations considerably decrease compared to cases shown in Figure 3(a,c). The critical Richardson numbers (their own for each Re) are close to those found in the flat surface case; however velocity and temperature fluctuations in the supercritical stratification remain finite even at large times.

Figure 4 shows the instantaneous vorticity modulus, $\omega(x,y,z)$, in different planes, obtained in DNS with $Re = 15\,000$ and $Ri = 0.04$, for $ka = 0.2$ and dimensionless wave phase velocity $c/U_0 = 0.05$ (corresponding to the wave age $c/u_* \approx 2$). The Obukhov length-scale, Eq. (23), is $L \approx 0.3$ and $Re_L \approx 300$, so that the Flores and Riley criterion, $Re_L > 100$, is satisfied. As illustrated, the flow is turbulent throughout the domain and exhibits numerous separation points and formation of Λ-shaped vortices (Moin and Kim, 1985) in the vicinity of the wave crests similar to those observed in DNS of non-stratified boundary-layer flow over a waved surface (Druzhinin *et al.*, 2012).

The supercritical regime observed in DNS with the same Reynolds number and wave slope and celerity but for $Ri = 0.08$ is presented in Figure 5. The figure shows that pre-turbulent fluctuations are quite pronounced in the vicinity of the waved surface, where the vorticity field exhibits complicated 3D structure, and these fluctuations decay sufficiently far from the surface.
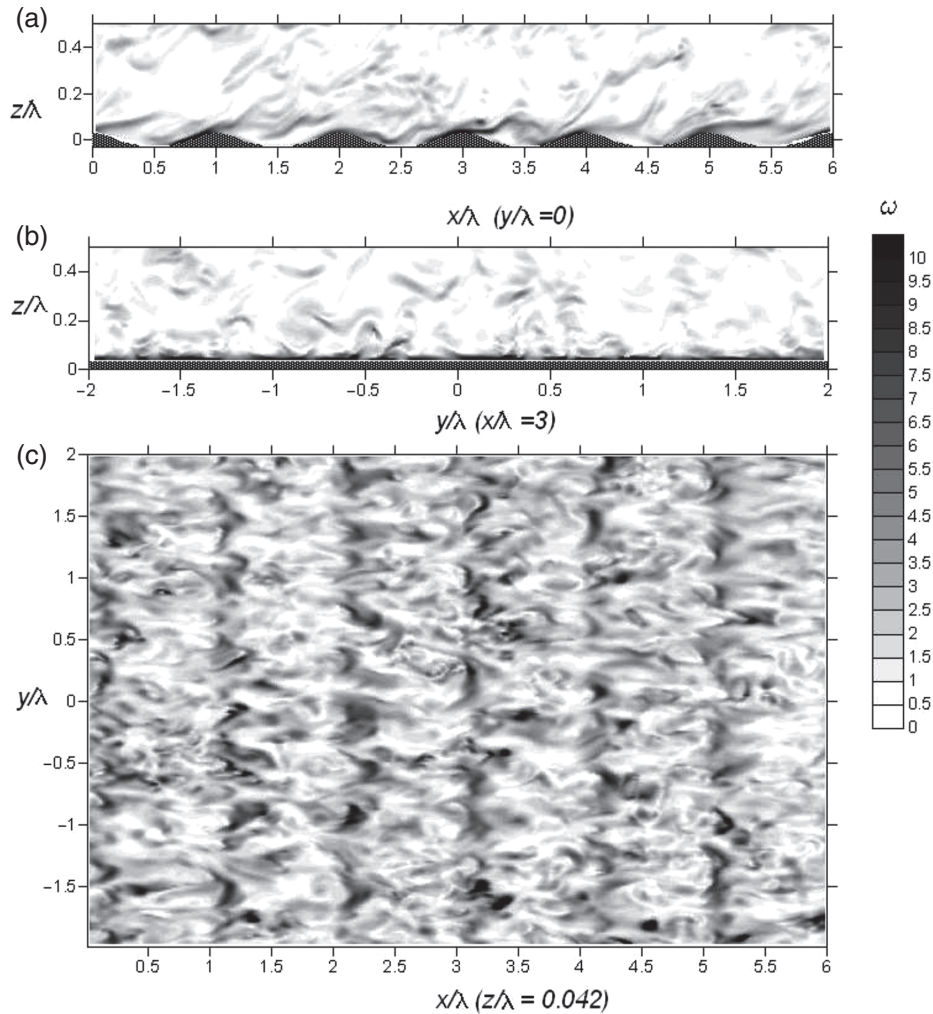
Figure 4. Instantaneous contours of the vorticity modulus in (a) *x-z*, (b) *y-z* and (c) *x-y* planes in statistically stationary, stably stratified boundary-layer flow over a waved surface with the wave slope $ka = 0.2$ and dimensionless phase velocity $c/U_0 = 0.05$ ($c/u_* \approx 2$), obtained in DNS for $Re = 15\,000$ and $Ri = 0.04$ at $t = 1000$. Level $z/\lambda = 0.042$ corresponds to $u_* z/\nu \approx 16$ and/or $z/L \approx 0.12$.

It follows that there is a principal difference between supercritically stratified ($\mathrm{Ri} > \mathrm{Ri_c}$) boundary-layer flows over the flat surface and waved surface. In the first case, supercritically stratified turbulence degenerates, and the flow becomes laminar. In the second case, turbulence also decreases under supercritical stratification, but finite velocity and temperature fluctuations survive near the surface-wave boundary and could affect the entire flow. These 'pre-turbulent' fluctuations manifest themselves most obviously in the vicinity of the critical layer, where the surface-wave phase velocity coincides with the mean flow velocity. The intensity of such fluctuations monotonically decreases with increasing bulk Richardson number. This supercritically stratified flow regime is studied in details in our follow-up study (Druzhinin *et al.* (2015), Part 2). Below we consider only stationary turbulent flow regimes.

4. Vertical profiles of the mean velocity and temperature

Our DNS produce vertical profiles of the mean velocity $U(\eta)$ and the deviation of mean temperature from its surface value, $(\Theta(\eta) - \Theta_1)$, which are in good agreement with the Monin-Obukhov similarity theory (cf. Monin and Yaglom, 1971). Figure 6 shows the profiles for $Re = 15\,000$, $Ri = 0.04$ and different wave slopes and phase velocities. The mean profiles are well described by the familiar approximation:

$$\frac{U(\eta)}{u_*} = \frac{1}{\kappa} \left(\ln \frac{\eta}{z_{0U}} + C_U \frac{\eta}{L} \right), \tag{26}$$

$$\frac{\Theta(\eta) - \Theta_0}{\Theta_*} = \frac{Pr_t}{\kappa} \left(\ln \frac{\eta}{z_{0\Theta}} + C_U \frac{\eta}{L} \right), \tag{27}$$

where z_{0U} and $z_{0\Theta}$ are effective roughness lengths, κ the von Kármán constant, C_U is one more empirical dimensionless constant, and Pr_t the turbulent Prandtl number. Results from DNS shown in Figure 6 yield practically the same estimates: $\kappa = 0.4$, $C_U = 2$ and $Pr_t = 0.85$ as observed in most laboratory and field experiments. We recall that our definition of the Obukhov length-scale L, Eq. (23), does not include the von Kármán constant, κ, whereas the popular version of this scale, $\widetilde{L}$, includes κ in the denominator, so that $\widetilde{L} = L/\kappa$. Then the second term on the right-hand side in brackets in Eqs (26) and (27) becomes $C_U \frac{\eta}{\kappa L} = \widetilde{C}_U \frac{\eta}{L}$ where $\widetilde{C}_U = \frac{C_U}{\kappa} = 5$.

As seen from Figure 6, increasing the wave slope ka leads to reducing the ratios U/u_* and $(\Theta - \Theta_0)/\Theta_*$. This is only natural, as the larger values of ka cause the larger roughness lengths z_{0U} and $z_{0\Theta}$, and therefore substantially larger u_* but only a bit larger Θ_*. The term $\sqrt{\tau} = u_*/U_0$ in the denominator on the r.h.s. of the second Eq. (22) just explains why the effect is less pronounced in the temperature profile.

Roughness lengths z_{00U} and $z_{00\Theta}$ for the flat surface are determined by conventional relations (e.g. Monin and Yaglom, 1971):

$$z_{00U} = \frac{\nu}{u_*} \exp(-5\kappa), \tag{28}$$

$$z_{00\Theta} = \frac{\nu}{u_*} \exp(-2.5\kappa). \tag{29}$$

For waved surfaces, we determined these parameters by matching Eqs (26) and (27) with DNS data and obtained essentially larger values: $z_{0U} = 2\, z_{00U}$ and $z_{0\Theta} = 1.5\, z_{00\Theta}$ at
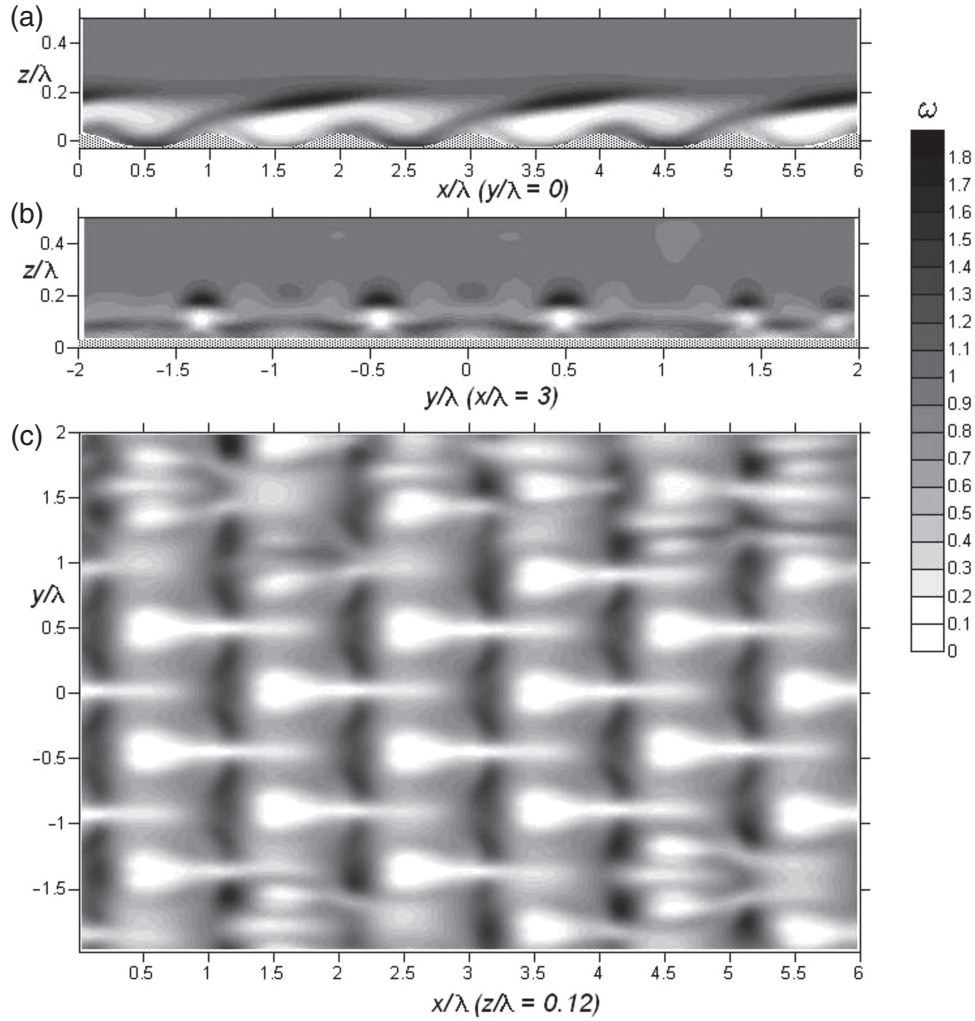
Figure 5. Instantaneous field of the vorticity modulus in (a) x-z plane at $y = 0$, (b) y-z plane at $x = 3$ and (c) x-y plane at $z = 0.12$, obtained from DNS of the wave-induced pre-turbulence in stably stratified boundary-layer flows for the bulk Reynolds number $Re = 15\,000$, bulk Richardson number $Ri = 0.08$, wave slope $ka = 0.2$, and dimensionless phase velocity $c/U_0 = 0.05$, at time $t = 1000$.

wave slope $ka = 0.1$; and $z_{0U} = 15\ z_{00U}$ and $z_{0\Theta} = 4\ z_{00\Theta}$ at $ka = 0.2$. DNSs also revealed that increasing phase velocity from $c/U_0 = 0.05$ to $c/U_0 = 0.2$ had no significant effects on mean profiles (Figure 6).

Good agreement with the Monin-Obukhov similarity theory laws analogous to Eqs (26) and (27), but with η denoting the height over a flat surface, was observed in many previous DNS studies of stably stratified turbulent boundary-layer flows (e.g. Nieuwstadt, 2005; Ansorge and Mellado, 2014; Deusebio *et al.*, 2014). In the present study we consider the same laws but use the *wave-following* coordinate, η, Eqs (4) and (5).

Figure 7 shows the turbulent Prandtl number

$$Pr_{\mathrm{t}} = \frac{u_*}{\Theta_*} \frac{\mathrm{d}\Theta}{\mathrm{d}\eta} \left(\frac{\mathrm{d}U}{\mathrm{d}\eta}\right)^{-1} \tag{30}$$

versus dimensionless height, $u_*\eta/\nu$, evaluated from DNS for different wave slopes and phase velocities. In all cases with $c/U_0 = 0.05$ (slow waves, e.g. Sullivan *et al.*, 2000; Yang and Shen, 2010), the general behaviour is as follows: in the vicinity of the water surface $Pr_{\mathrm{t}} \approx 1$, then it decreases and saturates at $Pr_{\mathrm{t}} \approx 0.85$ for $u_*\eta/\nu > 100$ (which corresponds in our DNS to $\eta/L > 0.3$). At phase velocity $c/U_0 = 0.2$ (intermediate waves), Pr_{t} is somewhat higher in the vicinity of the water surface (where it approaches about 1.2) but plateaus at the same approximate value ($Pr_{\mathrm{t}} \approx 0.85$) as for $c/U_0 = 0.05$. All the above features of mean profiles obtained from DNS agree well with the majority of known laboratory, numerical and field experiments.

5. Vertical fluxes of momentum and heat and root mean square fluctuations

Budgets of total vertical fluxes of momentum and heat are derived from the equations for the streamwise velocity component and the temperature deviation (cf. Appendix, Eqs (A5) and (A8)) by averaging over time and ξ_2-coordinate (along the wave front). Under the stationary turbulent regime, in the absence of a mean streamwise pressure gradient, the resulting equations are rewritten in curvilinear coordinates as follows:

$$\left\{\frac{\partial}{\partial \xi_1}\left(\frac{\partial x_1}{\partial \xi_1}\right) + \frac{\partial}{\partial \xi_3}\left(\frac{\partial x_1}{\partial \xi_3}\right)\right\}\langle U_1^2 + P\rangle$$
$$+ \left\{\frac{\partial}{\partial \xi_1}\left(\frac{\partial x_3}{\partial \xi_1}\right) + \frac{\partial}{\partial \xi_3}\left(\frac{\partial x_3}{\partial \xi_3}\right)\right\}\langle U_1 U_3\rangle$$
$$= \frac{1}{Re}\left(\frac{\partial^2}{\partial \xi_1^2} + \frac{\partial^2}{\partial \xi_3^2}\right)\langle U_1\rangle, \tag{31}$$

$$\left\{\frac{\partial}{\partial \xi_1}\left(\frac{\partial x_1}{\partial \xi_1}\right) + \frac{\partial}{\partial \xi_3}\left(\frac{\partial x_1}{\partial \xi_3}\right)\right\}\langle TU_1\rangle$$
$$+ \left\{\frac{\partial}{\partial \xi_1}\left(\frac{\partial x_3}{\partial \xi_1}\right) + \frac{\partial}{\partial \xi_3}\left(\frac{\partial x_3}{\partial \xi_3}\right)\right\}\langle TU_3\rangle$$
$$= \frac{1}{RePr}\left(\frac{\partial^2}{\partial \xi_1^2} + \frac{\partial^2}{\partial \xi_3^2}\right)\langle T\rangle, \tag{32}$$

where $T \equiv \widetilde{T} + \xi_3$. Now averaging Eqs (31) and (32) over ξ_1, taking into account periodicity over ξ_1 and ξ_2, and integrating over ξ_3 yields the following momentum-flux and heat-flux
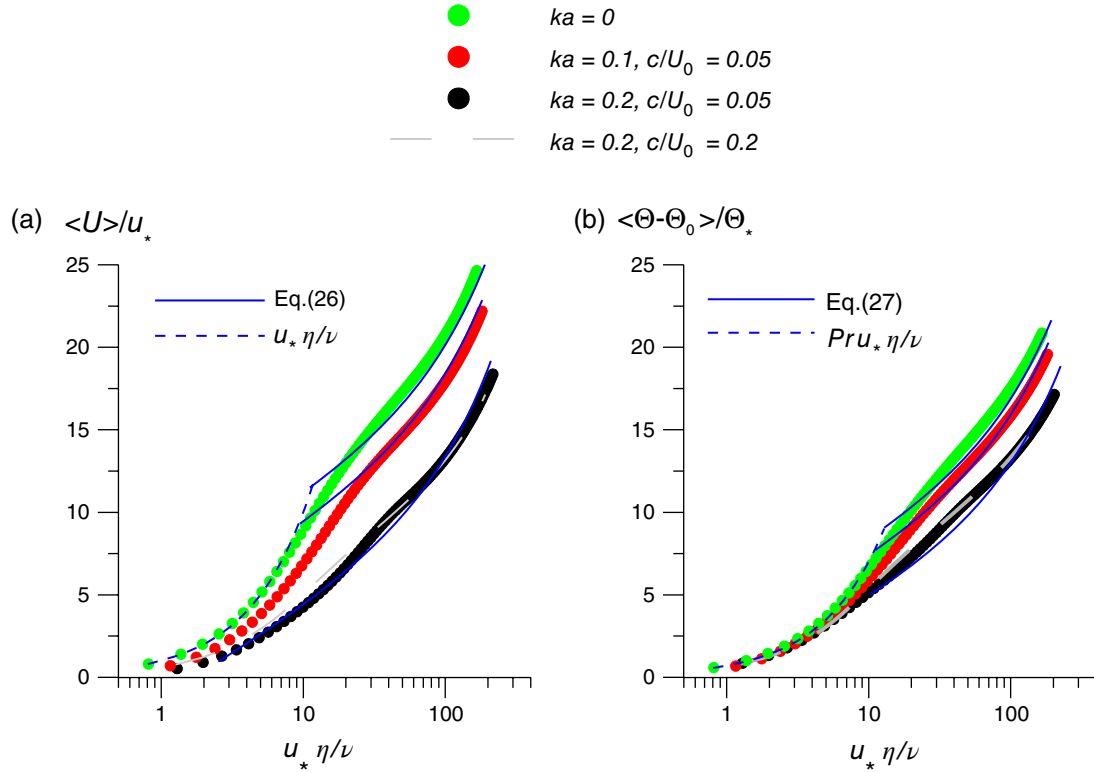
Figure 6. Vertical profiles of (a) the mean velocity and (b) temperature in the stationary turbulent boundary-layer flow over a waved water surface, obtained in DNS for $Re = 15\,000$ and $Ri = 0.04$ at different wave slopes ka, and dimensionless phase velocities c/U_0. The viscous-sublayer approximation and the log-linear approximation, Eqs (26) and (27), are shown by the dashed and the solid lines, respectively.
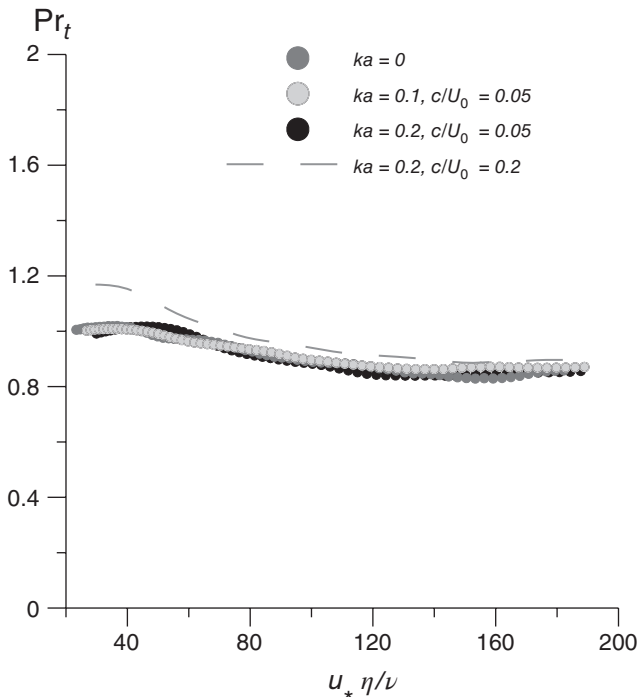

Figure 7. Vertical profiles of the turbulent Prandtl number, Pr_t, in stationary, turbulent boundary-layer flow over a waved water surface, obtained in DNS for $Re = 15\,000$ and $Ri = 0.04$ for different wave slopes ka, and dimensionless phase velocities c/U_0.

balance conditions:

$$\left[\frac{1}{Re}\frac{\partial\langle U_1\rangle}{\partial\xi_3} + \frac{\partial x_3}{\partial\xi_1}\langle U_1^2 + P\rangle - \frac{\partial x_3}{\partial\xi_3}\langle U_1 U_3\rangle\right] = \frac{u_*^2}{U_0^2}, \quad (33)$$

$$\left[\frac{1}{RePr}\frac{\partial\langle T\rangle}{\partial\xi_3} + \frac{\partial x_3}{\partial\xi_1}\langle TU_1\rangle - \frac{\partial x_3}{\partial\xi_3}\langle TU_3\rangle\right] = \frac{u_*\Theta_*}{U_0\Delta\Theta}, \quad (34)$$

where angular and square brackets denote phase-average and streamwise-average, respectively. Left-hand sides in Eqs (33) and (34) can be represented as sums of three contributions to total fluxes. In the dimensional form, these budgets read

$$\tau_t + \tau_v + \tau_w = u_*^2, \quad (35)$$

$$F_t + F_v + F_w = u_*\Theta_*, \quad (36)$$

where $\tau_t = U_0^2\tau$ and $F_t = U_0\Delta\Theta F$ are dimensional *turbulent* fluxes proportional to the dimensionless fluxes τ and F, Eqs (20) and (21); τ_v and F_v are *viscous* fluxes:

$$\tau_v = \frac{U_0^2}{Re}\frac{d[\langle U_1\rangle]}{d\eta}, \quad (37)$$

$$F_v = \frac{U_0\Delta\Theta}{RePr}\frac{d[\langle T\rangle]}{d\eta}. \quad (38)$$

Finally *wave-induced* fluxes, τ_w and F_w, are obtained as respective residual contributions on the left-hand side of Eqs (34) and (35) as:

$$\tau_w = U_0^2\left[\frac{\partial x_3}{\partial\xi_1}\langle U_1^2 + P\rangle - \left(\frac{\partial x_3}{\partial\xi_3} - 1\right)\langle U_1 U_3\rangle - \langle U_1\rangle\langle U_3\rangle\right], \quad (39)$$

$$F_w = U_0\Delta\Theta\left[\frac{\partial x_3}{\partial\xi_1}\langle TU_1\rangle - \left(\frac{\partial x_3}{\partial\xi_3} - 1\right)\langle TU_3\rangle - \langle T\rangle\langle U_3\rangle\right]. \quad (40)$$

Figure 8 shows the shares of all three components to the total vertical fluxes of momentum and heat obtained in DNS of stationary turbulent boundary-layer flow at $Re = 15\,000$ and $Ri = 0.04$ for different wave slopes and phase velocities. For wave slope $ka = 0.2$, the wave-induced flux of momentum, τ_w, at the water surface nearly equals the viscous stress, τ_v, which means that the form drag equals the viscous drag. For $ka = 0.1$, the wave-induced flux at the water surface is about three times smaller than
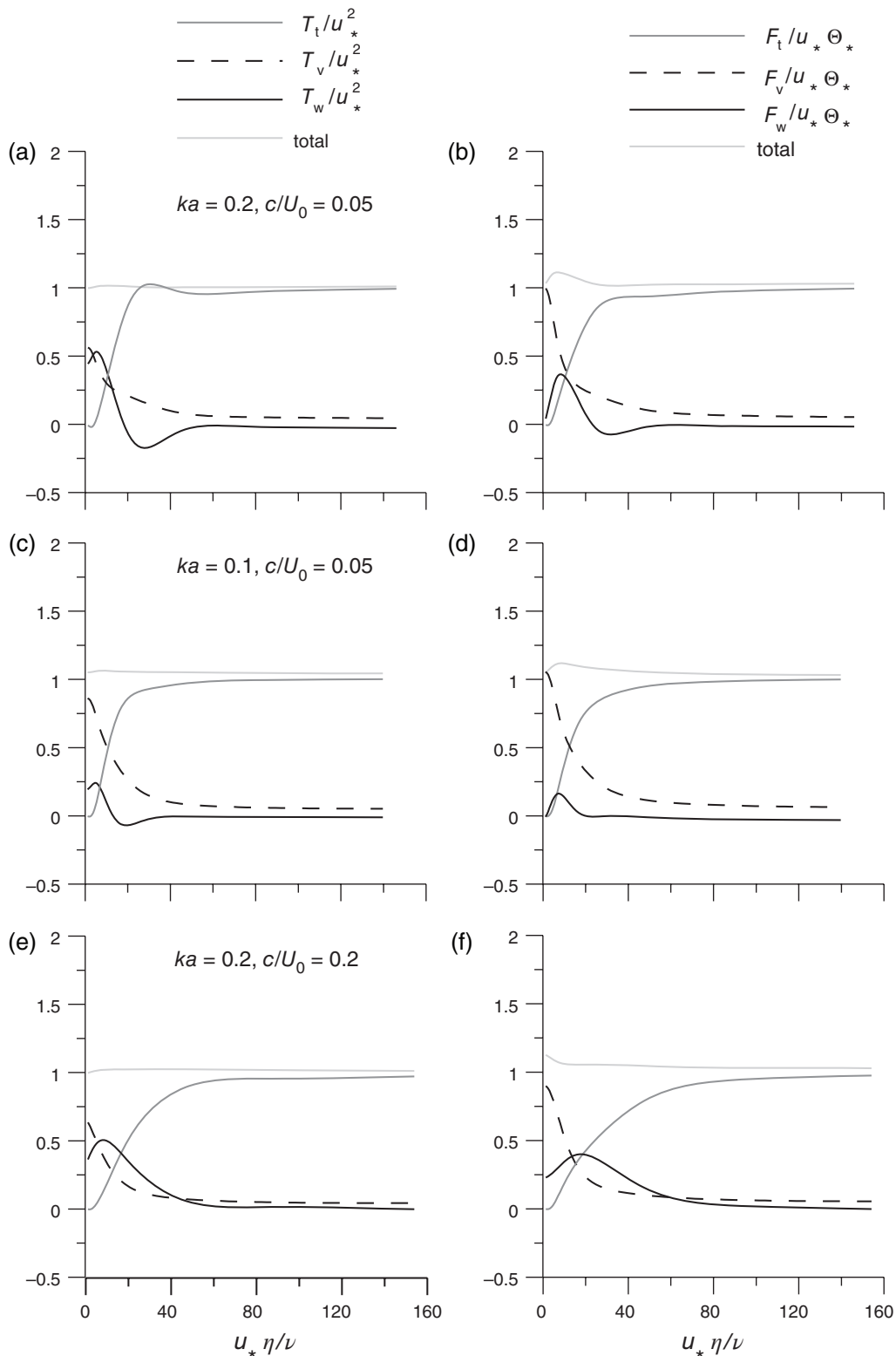
Figure 8. Turbulent, viscous and wave-induced shares of the total vertical fluxes of (a, c, e) momentum and (b, d, f) heat in stably stratified boundary-layer flows over waved surfaces with (a, b) $ka = 0.2$, $c/U_0 = 0.05$, $c/u_* \approx 2$; (c, d) $ka = 0.1$, $c/U_0 = 0.05$, $c/u_* \approx 2$; and (e, f) $ka = 0.2$, $c/U_0 = 0.2$, $c/u_* \approx 8$ in DNS for $Re = 15\,000$ and $Ri = 0.04$.

the viscous stress. Both τ_w and τ_v become negligible compared to the turbulent flux, τ_t, sufficiently far from the surface, at $u_*\eta/\nu > 40$.

The wave-induced heat flux, F_w, for wave slope $ka = 0.2$ is negligible compared to the molecular heat flux, F_v, in the vicinity of the waved surface (at $u_*\eta/\nu < 10$). With increasing height, F_w increases and becomes of the same order as F_v: at $u_*\eta/\nu \approx 10$ for phase velocity $c/U_0 = 0.05$, and at $u_*\eta/\nu \approx 20$ for $c/U_0 = 0.2$. For wave slope $ka = 0.1$, the wave-induced heat flux is negligible compared to the turbulent and viscous heat fluxes, F_t and F_v. Similarly to the wave-induced and the viscous fluxes

of momentum, heat fluxes F_w and F_v both return to 0 sufficiently far from the surface.

Results from DNS of airflows over flat and waved boundaries for different bulk Richardson numbers shown in Figure 9 demonstrate how the wave phase velocity, wave slope and stable stratification affect vertical profiles of turbulent fluxes of momentum and heat. The fluxes are generally enhanced by surface waves with larger slope ka, and weakened by strengthening stratification and increasing wave phase velocity.

Figure 10 presents vertical profiles of the mean velocity and temperature gradients, $dU/d\eta$ and $d\Theta/d\eta$, and the root mean
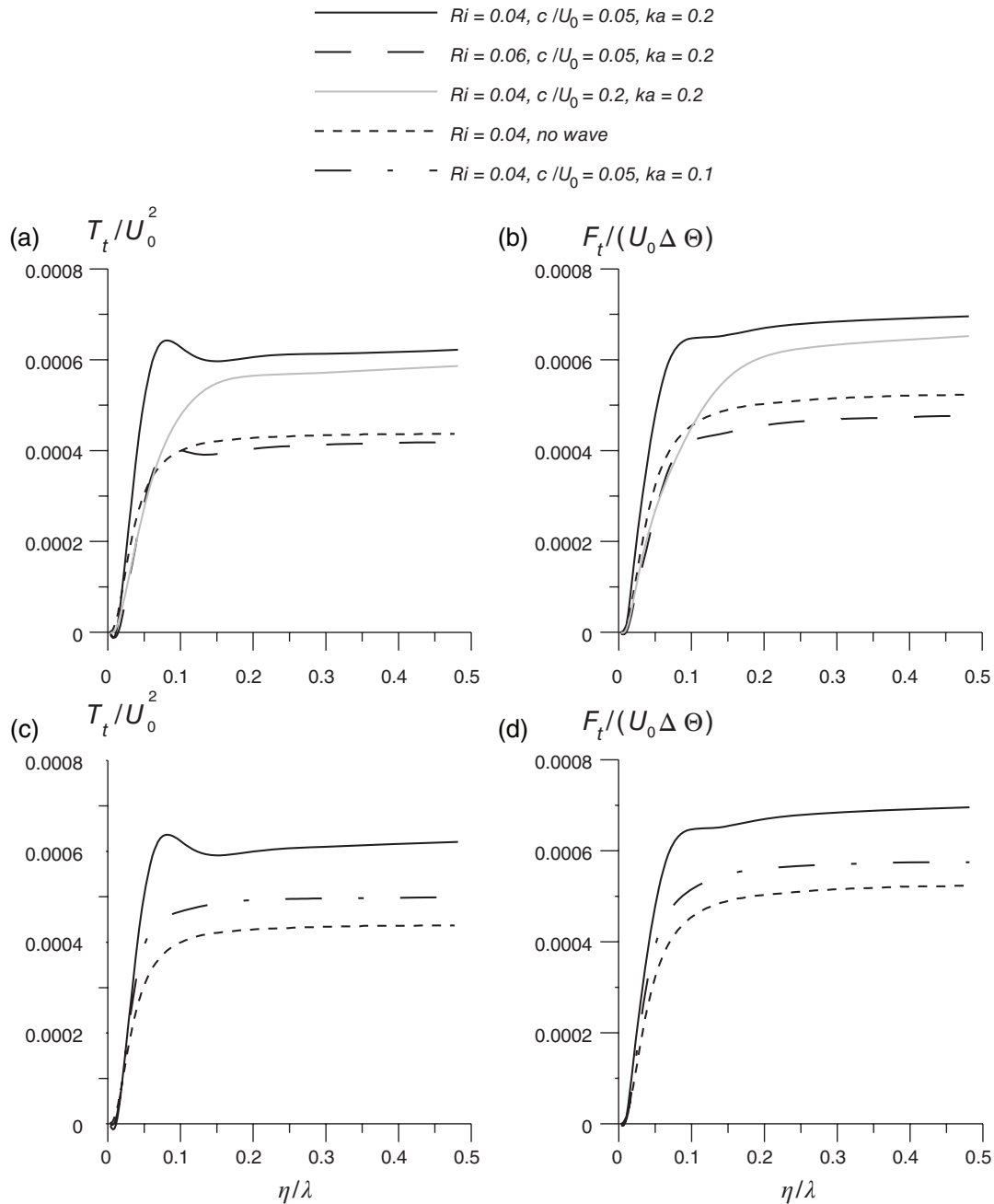
Figure 9. Profiles of (a, c) turbulent momentum and (b, d) heat fluxes, τ_t and F_t, obtained in DNS with $Re = 15\,000$ under the stationary turbulent regime of stably stratified boundary-layer flow over a waved surface for different slopes ka, phase velocities c/U_0, and bulk Richardson numbers Ri. The profiles obtained for the flat boundary case (no wave, with $ka = 0$) with $Ri = 0.04$ are also provided for comparison.

square velocity and temperature fluctuations, (U', V', W') and (Θ'), Eq. (25), obtained in DNS of the stationary turbulent regime at $Ri = 0.04$. The fluctuations are obviously enhanced at larger wave slope, whereas the velocity and temperature gradients remain unaffected in the bulk of the flow domain – outside the viscous and buffer layers (at $\eta/\lambda > 0.1$). Hence the root mean square fluctuations, as well as turbulent fluxes, substantially increase with increasing wave slope, whereas the gradients of mean velocity and temperature remain practically the same. It follows that the enhancement of turbulence is originated by the surface wave rather than by the shear instability of the mean flow. The enhancement of the turbulent flux of momentum by larger wave slope is also due to larger form drag (cf. Figure 9). It deserves emphasising that the heat flux is also increased by the surface wave, in spite of no thermal analogue to the form drag.

Results from our DNS offered a clearer view on the difference between the regimes of real turbulence and weak turbulence-like motions, which occurred in two numerical experiments for same wave slope $ka = 0.2$ but different bulk Reynolds numbers $Re = 15\,000$ and $40\,000$. Similarly to Flores and Riley (2011) and

to our analyses of the airflows over a flat surface, we determined for each Re the critical bulk Richardson number Ri_c, such that for $Ri < Ri_c$ the flow remains turbulent but for larger Ri turbulence decays (cf. Figure 3). At the same time, over the waved surface the situation is more complicated. Figure 11 1shows vertical profiles of the turbulent Reynolds number Re_L, Eq. (24), for the bulk Richardson number just below the critical value at $Re = 15\,000$ and $40\,000$. The figure reveals almost the same threshold value of $Re_L \sim 100$ as for the flows over a flat surface (cf. Figure 2). However, in supercritically stratified airflows over waves, the latter excite in the airflow weak 'pre-turbulent' motions, which neither decay nor develop into real turbulence (cf. Figure 3). We consider this newly recognised regime in more detail in the follow-up article (Druzhinin *et al.*, 2015).

6. Conclusions

This article summarises results obtained by direct numerical simulation (DNS) of stably stratified turbulent boundary-layer
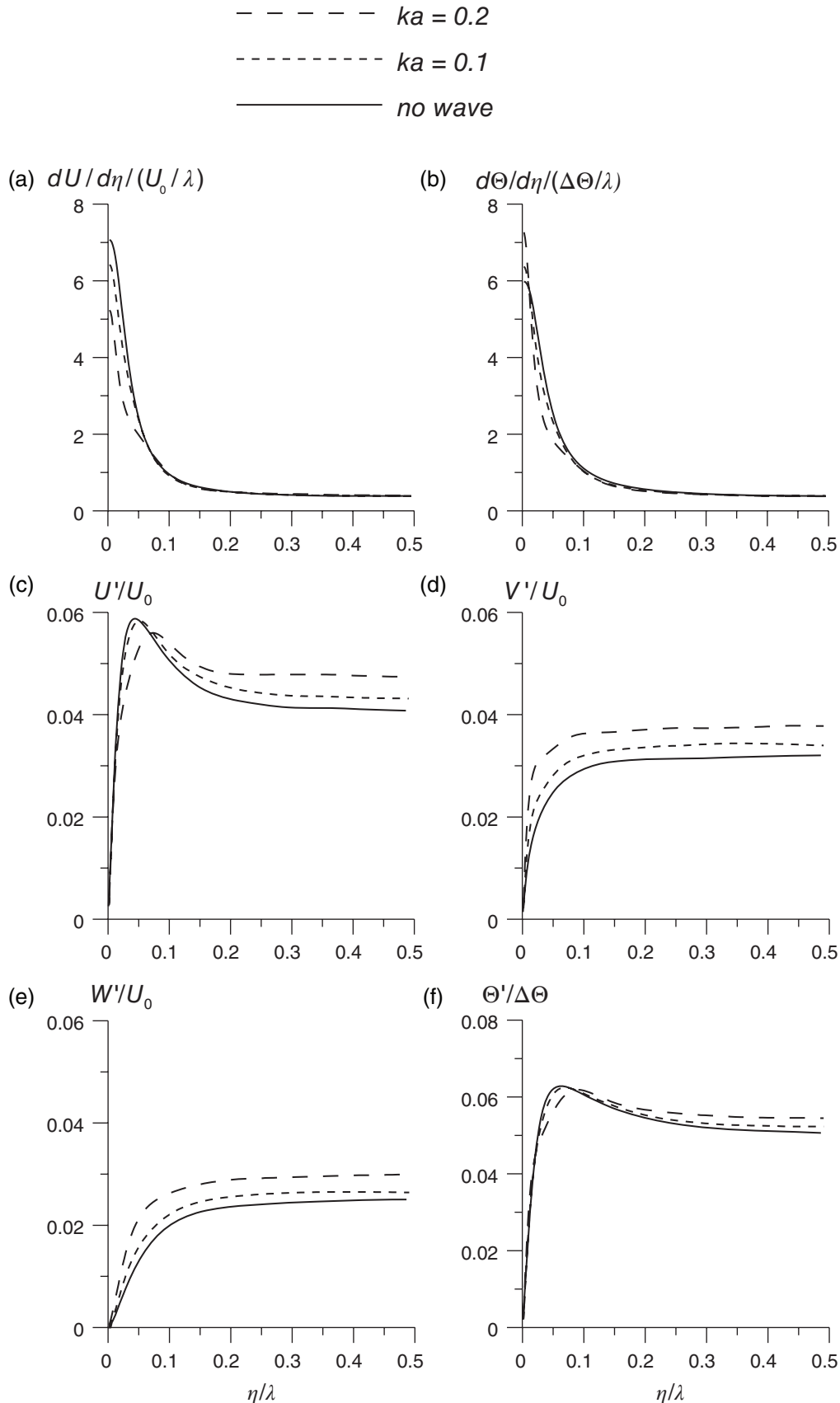
Figure 10. Vertical profiles of mean gradients of (a) velocity dU/dz, (b) temperature $d\Theta/dz$, and root mean square fluctuations of velocity, (c) U', (d) V', (e) W', and (f) temperature Θ', in DNS of stably stratified turbulent boundary-layer flows over waved surfaces with $c/U_0 = 0.05$ ($c/u_* \approx 2$) and two different wave slopes ($ka = 0.2$ and $ka = 0.1$) and over a flat surface ($c/U_0 = 0$ and $ka = 0$), for $Re = 15\,000$ and $Ri = 0.04$.

flow over flat and waved water surfaces. In the statistically stationary, turbulent regime observed in DNS for not too large bulk Richardson numbers, the simulated mean velocity and temperature profiles, Eqs (26) and (27), are quite similar to the log-linear profiles observed in the atmospheric surface layer. Moreover, the turbulent Prandtl number Pr_t, von Kármán

constant κ, and dimensionless constant C_U in the linear term are practically the same as in the atmosphere and DNS: $\kappa = 0.4$, $Pr_t = 0.85$, and $C_U = 2$.

The wind and temperature roughness lengths, z_{0U} and $z_{0\Theta}$, obtained from DNS, increase with the increasing surface wave slope. For z_{0U}, this effect is well-known and easily explained
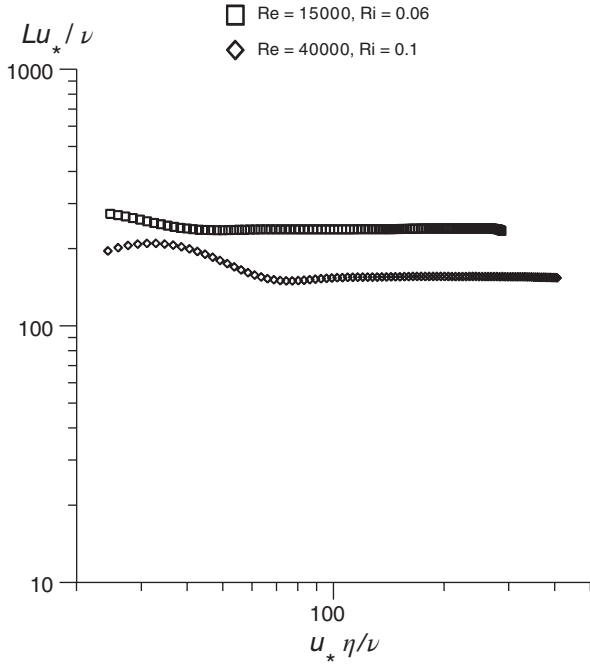
Figure 11. Vertical profiles of the Reynolds number Re_L in DNS of stably stratified boundary-layer flow over a waved surface with slope $ka = 0.2$ for different bulk Reynolds and Richardson numbers.

by the form drag. DNS clearly show the similar (although less pronounced) effect for $z_{0\Theta}$. This important fact deserves attention because the heat-transfer mechanisms have no visible similarity to the form-drag mechanism.

Results from our DNS offer a clearer view of the viscous/molecular, turbulent and wave-induced contributions to the vertical turbulent fluxes of momentum and heat at different elevations over the water surface for different wave slopes and phase velocities. To the best of our knowledge, such quantitative analyses have not been performed previously.

Comparative analyses of the mean velocity and temperature gradients and turbulent velocity and temperature fluctuations obtained in DNS reveal that the increasing wave slope enhances turbulent fluctuations but does not affect mean velocity and temperature gradients. It follows that the observed enhancement of turbulence is caused directly by the surface waves rather than indirectly by the mean-flow instability.

Our DNS results confirm the Flores and Riley (2011) criterion of transition from turbulent to laminar regime over a flat surface, namely the turbulent Reynolds number $Re_L = u_* L/(\kappa \nu)$ with the threshold value $Re_L^{\text{th}} \approx 10^2$. Our DNS reveal precisely the same threshold over waved surfaces, but with important proviso: over steep waves $Re_L^{\text{th}} \approx 10^2$ separates the regimes of real turbulence and 'pre-turbulent' wave-induced motions most pronounced in the vicinity of the water surface.

Acknowledgements

A.   Appendix: Governing equations in curvilinear coordinates.

We define dimensionless Cartesian coordinates as $x_1 = x/\lambda$, $x_2 = y/\lambda$, $x_3 = z/\lambda$. Then, due to the conformal properties of the mapping, Eqs (4) and (5), the following relationships hold:

$$\frac{\partial \xi_1}{\partial x_1} = \frac{\partial \xi_3}{\partial x_3} = \frac{1}{J}\frac{\partial x_1}{\partial \xi_1} = \frac{1}{J}\frac{\partial x_3}{\partial \xi_3}, \tag{A1}$$

$$\frac{\partial \xi_1}{\partial x_3} = -\frac{\partial \xi_3}{\partial x_1} = \frac{1}{J}\frac{\partial x_3}{\partial \xi_1} = -\frac{1}{J}\frac{\partial x_1}{\partial \xi_3}, \tag{A2}$$

where $J = \left(\frac{\partial x_1}{\partial \xi_1}\right)^2 + \left(\frac{\partial x_1}{\partial \xi_3}\right)^2$ is the Jacobian of the mapping. The derivatives over x_1 and x_3 are replaced by the derivatives over ξ_1 and ξ_3:

$$\frac{\partial}{\partial x_1} = \frac{1}{J}\left\{\frac{\partial}{\partial \xi_1}\left(\frac{\partial x_1}{\partial \xi_1}\right) + \frac{\partial}{\partial \xi_3}\left(\frac{\partial x_1}{\partial \xi_3}\right)\right\},$$
$$\frac{\partial}{\partial x_3} = \frac{1}{J}\left\{\frac{\partial}{\partial \xi_1}\left(\frac{\partial x_3}{\partial \xi_1}\right) + \frac{\partial}{\partial \xi_3}\left(\frac{\partial x_3}{\partial \xi_3}\right)\right\}, \tag{A3}$$

and the Laplacian operator in curvilinear coordinates becomes

$$\frac{\partial^2}{\partial x_j \partial x_j} = \frac{1}{J}\left(\frac{\partial^2}{\partial \xi_1^2} + \frac{\partial^2}{\partial \xi_3^2}\right) + \frac{\partial^2}{\partial \xi_2^2}. \tag{A4}$$

Using Eqs (A1)−(A4), the governing Navier-Stokes equations for the dimensionless velocity components $U_{1,2,3}$ and temperature deviation $\widetilde{T}$ can be written in dimensionless curvilinear coordinates:

$$\frac{\partial U_1}{\partial t} + \frac{1}{J}\left\{\frac{\partial}{\partial \xi_1}\left(\frac{\partial x_1}{\partial \xi_1}U_1^2\right) + \frac{\partial}{\partial \xi_3}\left(\frac{\partial x_1}{\partial \xi_3}U_1^2\right) + \frac{\partial}{\partial \xi_1}\left(\frac{\partial x_3}{\partial \xi_1}U_1 U_3\right)\right.$$
$$\left. + \frac{\partial}{\partial \xi_3}\left(\frac{\partial x_3}{\partial \xi_3}U_1 U_3\right)\right\} + \frac{\partial (U_1 U_2)}{\partial \xi_2}$$
$$= -\frac{1}{J}\left\{\frac{\partial}{\partial \xi_1}\left(\frac{\partial x_1}{\partial \xi_1}P\right) + \frac{\partial}{\partial \xi_3}\left(\frac{\partial x_1}{\partial \xi_3}P\right)\right\}$$
$$+ \frac{1}{Re}\left\{\frac{1}{J}\left(\frac{\partial^2 U_1}{\partial \xi_1^2} + \frac{\partial^2 U_1}{\partial \xi_3^2}\right) + \frac{\partial^2 U_1}{\partial \xi_2^2}\right\} \tag{A5}$$

$$\frac{\partial U_2}{\partial t} + \frac{1}{J}\left\{\frac{\partial}{\partial \xi_1}\left(\frac{\partial x_1}{\partial \xi_1}U_1 U_2\right) + \frac{\partial}{\partial \xi_3}\left(\frac{\partial x_1}{\partial \xi_3}U_1 U_2\right)\right.$$
$$\left. + \frac{\partial}{\partial \xi_1}\left(\frac{\partial x_3}{\partial \xi_1}U_2 U_3\right) + \frac{\partial}{\partial \xi_3}\left(\frac{\partial x_3}{\partial \xi_3}U_2 U_3\right)\right\} + \frac{\partial U_2^2}{\partial \xi_2}$$
$$= -\frac{\partial P}{\partial \xi_2} + \frac{1}{Re}\left\{\frac{1}{J}\left(\frac{\partial^2 U_2}{\partial \xi_1^2} + \frac{\partial^2 U_2}{\partial \xi_3^2}\right) + \frac{\partial^2 U_2}{\partial \xi_2^2}\right\} \tag{A6}$$

$$\frac{\partial U_3}{\partial t} + \frac{1}{J}\left\{\frac{\partial}{\partial \xi_1}\left(\frac{\partial x_1}{\partial \xi_1}U_1 U_3\right) + \frac{\partial}{\partial \xi_3}\left(\frac{\partial x_1}{\partial \xi_3}U_1 U_3\right)\right.$$
$$\left. + \frac{\partial}{\partial \xi_1}\left(\frac{\partial x_3}{\partial \xi_1}U_3^2\right) + \frac{\partial}{\partial \xi_3}\left(\frac{\partial x_3}{\partial \xi_3}U_3^2\right)\right\} + \frac{\partial (U_2 U_3)}{\partial \xi_2}$$
$$= -\frac{1}{J}\left\{\frac{\partial}{\partial \xi_1}\left(\frac{\partial x_3}{\partial \xi_1}P\right) + \frac{\partial}{\partial \xi_3}\left(\frac{\partial x_3}{\partial \xi_3}P\right)\right\}$$
$$+ \frac{1}{Re}\left\{\frac{1}{J}\left(\frac{\partial^2 U_3}{\partial \xi_1^2} + \frac{\partial^2 U_3}{\partial \xi_3^2}\right) + \frac{\partial^2 U_3}{\partial \xi_2^2}\right\} + \delta_{iz}Ri\widetilde{T}f(t) \tag{A7}$$

$$\frac{\partial \widetilde{T}}{\partial t} + \frac{1}{J}\left\{\frac{\partial}{\partial \xi_1}\left(\frac{\partial x_1}{\partial \xi_1}U_1\widetilde{T}\right) + \frac{\partial}{\partial \xi_3}\left(\frac{\partial x_1}{\partial \xi_3}U_1\widetilde{T}\right)\right.$$
$$\left. + \frac{\partial}{\partial \xi_1}\left(\frac{\partial x_3}{\partial \xi_1}U_3\widetilde{T}\right) + \frac{\partial}{\partial \xi_3}\left(\frac{\partial x_3}{\partial \xi_3}U_3\widetilde{T}\right)\right\} + \frac{\partial (U_2\widetilde{T})}{\partial \xi_2}$$
$$= -\frac{1}{J}\left(U_1\frac{\partial x_3}{\partial \xi_1} + U_3\frac{\partial x_3}{\partial \xi_3}\right) + \frac{1}{RePr}\left\{\frac{1}{J}\left(\frac{\partial^2 \widetilde{T}}{\partial \xi_1^2} + \frac{\partial^2 \widetilde{T}}{\partial \xi_3^2}\right) + \frac{\partial^2 \widetilde{T}}{\partial \xi_2^2}\right\} \tag{A8}$$

We introduce the factor f in the last term on the right hand site of Eq. (A7) in the form

$$f(t) = 1 - \exp(-t/100), \quad (A9)$$

where t is the dimensionless time. The function $f(t)$ 'switches on' the buoyancy force and the related stabilizing effect of stratification at times $t \gg 100$, so that the non-stratified turbulent Couette flow regime is allowed to develop at times $t < 100$.

Following Druzhinin et al. (2012), we also employ mapping over the vertical coordinate:

$$\xi_3 = 0.5 \left(1 + \frac{\tanh \widetilde{\eta}}{\tanh 1.5} \right), \quad (A10)$$

where $-1.5 < \widetilde{\eta} < 1.5$. Equation (A10) introduces non-uniform spacing of computational nodes in the vertical direction, with stretching in the middle of the domain (for $\widetilde{\eta} \approx 0$ and $x_3 \approx \xi_3 \approx 0.5$) and clustering near the boundaries (for $\widetilde{\eta} \approx \pm 1.5$ and $x_3 \approx \xi_3 \approx 0$ or 1). Due to Eq. (A10), the derivative over compressed curvilinear coordinate $\widetilde{\eta}$ is expressed via the derivative over ξ_3:

$$\frac{\partial}{\partial \xi_3} = 2 \tanh 1.5 \cosh \widetilde{\eta} \frac{\partial}{\partial \widetilde{\eta}}. \quad (A11)$$

Integration of Eqs (A5)–(A8) is advanced in time by the second-order accuracy Adams-Bashforth method in two stages at each time step n. To calculate the wind velocity at the new $(n+1)$ time step, firstly an intermediate velocity, $\breve{U}_i$, is calculated using the velocity and the temperature deviation obtained at the preceding time steps, $(U_i^{n-1}, \widetilde{T}^{n-1})$ and $(U_i^n, \widetilde{T}^n)$:

$$\widetilde{U}_i = U_i^n + \left(\frac{3}{2} F_i^U \left(U_i^n, \widetilde{T}^n, t_n \right) - \frac{1}{2} F_i^U (U_i^{n-1}, \widetilde{T}^{n-1}, t_n) \right) \Delta t. \quad (A12)$$

Then the flux $F^T(U_i, \widetilde{T}, t)$ is calculated:

$$F_i(U_i, \widetilde{T}, t) = -\frac{\partial (U_i U_j)}{\partial x_j} + \frac{1}{Re} \frac{\partial^2 U_i}{\partial x_j \partial x_j} + \delta_{iz} Ri \widetilde{T} f(t). \quad (A13)$$

Here and below in Eqs (A14)–(A19), we use for brevity the derivatives over Cartesian coordinates x_1 and x_3, which are readily expressed in the same manner as in Eqs (A1)–(A3) via the derivatives over curvilinear coordinates ξ_1 and ξ_3; and the Laplacian operator is rewritten in the same manner in Eq. (A4). Then, the air pressure at the $n+1$ time step is obtained by solving the Poisson equation:

$$\frac{\partial^2 P^{n+1}}{\partial x_j \partial x_j} = \frac{1}{\Delta t} \frac{\partial \widetilde{U}_j}{\partial x_j}, \quad (A14)$$

where the velocity divergence on the r.h.s. in curvilinear coordinates reads:

$$\frac{\partial \widetilde{U}_j}{\partial x_j} = \frac{1}{J} \left\{ \frac{\partial}{\partial \xi_1} \left(\frac{\partial x_1}{\partial \xi_1} \widetilde{U}_1 \right) + \frac{\partial}{\partial \xi_3} \left(\frac{\partial x_1}{\partial \xi_3} \widetilde{U}_1 \right) \right.$$
$$\left. + \frac{\partial}{\partial \xi_1} \left(\frac{\partial x_3}{\partial \xi_1} \widetilde{U}_3 \right) + \frac{\partial}{\partial \xi_3} \left(\frac{\partial x_3}{\partial \xi_3} \widetilde{U}_3 \right) \right\} + \frac{\partial \widetilde{U}_2}{\partial \xi_2}. \quad (A15)$$

The pressure equation

$$\left(\frac{\partial^2}{\partial \xi_1^2} + \frac{\partial^2}{\partial \xi_2^2} + \frac{\partial^2}{\partial \xi_3^2} \right) P_k^{n+1} = \frac{1}{J} \frac{\partial \widetilde{U}_j}{\partial x_j} + \left(1 - \frac{1}{J} \right) \frac{\partial^2 P_{k-1}^{n+1}}{\partial \xi_3^2} \quad (A16)$$

is solved by iterations (k is the iteration number) employing the fast Fourier transform over ξ_1, ξ_2 coordinates and the Gauss elimination method over the ξ_3-coordinate. The iteration procedure stops when the condition $\max\{|P_k - P_{k-1}|/|P_{k-1}|\} < 0.01$ is satisfied. Usually this condition is reached after three to five iterations (Druzhinin et al., 2012). Then new velocity at $n+1$ time step, satisfying the incompressibility condition, Eq. (2), is calculated:

$$U_i^{n+1} = \widetilde{U}_i - \frac{\partial P^{n+1}}{\partial x_j} \Delta t. \quad (A17)$$

The temperature deviation at a new $(n+1)$ time step is calculated using data from the previous step:

$$\widetilde{T}^{n+1} = \widetilde{T}^n + \left(\frac{3}{2} F_T \left(U_i^n, \widetilde{T}^n \right) - \frac{1}{2} F_T (U_i^{n-1}, \widetilde{T}^{n-1}) \right) \Delta t, \quad (A18)$$

where $F_T(U_i, \widetilde{T})$ is the temperature flux:

$$F_T(U_i, \widetilde{T}) = -\frac{\partial (U_j \widetilde{T})}{\partial x_j} - U_z + \frac{1}{PrRe} \frac{\partial^2 \widetilde{T}}{\partial x_j \partial x_j}. \quad (A19)$$

References

Adrian RJ. 1991. Particle imaging techniques for experimental fluid dynamics. *Annu. Rev. Fluid Mech.* **23**: 261–304.

Al-Zanaidi MA, Hui WH. 1984. Turbulent airflow over water waves – a numerical study. *J. Fluid Mech.* **148**: 225–246.

Ansorge C, Mellado J-P. 2014. Global intermittency and collapsing turbulence in the stratified planetary boundary layer. *Boundary-Layer Meteorol.* **153**: 89–116, doi: 10.1007/s10546-014- 9941-3.

Chalikov DV. 1986. Numerical simulation of the boundary layer above water waves. *Boundary-Layer Meteorol.* **34**: 63–98.

Coleman GN, Ferziger JH, Spalart PR. 1992. Direct simulation of the stably stratified turbulent Ekman layer. *J. Fluid Mech.* **244**: 677–712.

Deusebio E, Brethouwer G, Schlatter P, Lindborg E. 2014. A numerical study of the unstratified and stratified Ekman layer. *J. Fluid Mech.* **755**: 672–704, doi: 10.1017/jfm.2014.318.

Donelan MA, Babanin AV, Young IR, Banner ML, McCormick C. 2005. Wave follower field measurements of the wind input spectral function Part. I: Measurements and calibrations. *J. Atmos. Oceanic Technol.* **22**: 799–813.

Druzhinin OA, Troitskaya YI, Zilitinkevich SS. 2012. Direct numerical simulation of a turbulent wind over a wavy water surface. *J. Geophys. Res.* **117**: C00J05, doi: 10.1029/2011JC007789.

Druzhinin OA, Troitskaya YI, Zilitinkevich SS. 2015. Stably stratified airflow over a waved water surface. Part 2: Wave-induced pre-turbulent motions. *Q. J. R. Meteorol. Soc.*, doi: 10.1002/qj.2678.

Fairall CW, Bradley EF, Hare JE. 2003. Bulk parameterization of air-sea fluxes: Updates and verification for the COARE algorithm. *J. Clim.* **16**: 571–591.

Flores O, Riley JJ. 2011. Analysis of turbulence collapse in the stably stratified surface layer using direct numerical simulation. *Boundary-Layer Meteorol.* **139**: 241–259.

García-Villalba M, del Álamo JC. 2011. Turbulence modification by stable stratification in channel flow. *Phys. Fluids* **23**: 045104-1–045104-22, doi: 10.1063/1.3560359.

Gent PR, Taylor PA. 1976. A numerical model of the air flow above water waves. *J. Fluid Mech.* **77**: 105–128.

Hsu CT, Hsu EY. 1983. On the structure of turbulent flow over a progressive water wave: Theory and experiment in a transformed wave-following coordinate system. Part 2. *J. Fluid Mech.* **131**: 123–153.

Hsu CT, Hsu EY, Street RL. 1981. On the structure of turbulent flow over a progressive water wave: Theory and experiment in a transformed, wave-following co-ordinate system. *J. Fluid Mech.* **105**: 87–117.

L'vov VS, Pomyalov A, Procaccia I, Zilitinkevich SS. 2006. Phenomenology of wall bounded Newtonian turbulence. *Phys. Rev. E* **73**: 1–13.

Moin P, Kim J. 1985. The structure of the vorticity field in the turbulent channel flow. Part 1. Analysis of instantaneous fields and statistical correlations. *J. Fluid Mech.* **155**: 441–464.

Moin P, Manesh K. 1998. Direct numerical simulation: a tool in turbulence research. *Annu. Rev. Fluid Mech.* **30**: 539–578.

Monin AS, Yaglom AM. 1971. *Statistical Fluid Mechanics: Mechanics of Turbulence*, Vol. **1**. MIT Press: Cambridge, MA, and London, UK.

Nieuwstadt FTM. 2005. Direct numerical simulation of stable channel flow at large stability. *Boundary-Layer Meteorol.* **116**: 277–299, doi: 10.1007/s10546-004-2818-0.

Pope SB. 2000. *Turbulent Flows*. Cambridge University Press: Cambridge, UK.

Reul N, Branger H, Giovanangeli J-P. 1999. Air flow separation over unsteady breaking waves. *Phys. Fluids.* **11**: 1959–1961.

Sullivan PP, McWilliams JC. 2002. Turbulent flow over water waves in the presence of stratification. *Phys. Fluids* **14**: 1182–1195.

Sullivan PP, McWilliams JC, Moeng C-H. 2000. Simulation of turbulent flow over idealized water waves. *J. Fluid Mech.* **404**: 47–85.

Sullivan PP, Edson J, Hristov T, McWilliams JC. 2008. Large-eddy simulations and observations of atmospheric marine boundary layers above non-equilibrium surface waves. *J. Atmos. Sci.* **65**: 1225–1245.

Sullivan PP, McWilliams JC, Patton EG. 2014. Large-eddy simulation of marine atmospheric boundary layers above a spectrum of moving waves. *J. Atmos. Sci.* **68**: 2395–2415.

Troitskaya Y, Sergeev D, Ermakova O, Balandina G. 2011. Statistical parameters of the air turbulent boundary layer over steep water waves measured by the PIV technique. *J. Phys. Oceanogr.* **41**: 1421–1454.

Veron F, Saxena G, Misra SK. 2007. Measurements of the viscous tangential stress in the airflow above wind waves. *Geophys. Res. Lett.* **34**: L19603, doi: 10.1029/2007GL031242.

Yang D, Shen L. 2010. Direct-simulation-based study of turbulent flow over various waving boundaries. *J. Fluid Mech.* **650**: 131–180.